



# Biopolymer templated strategized greener protocols for fabrication of ZnO nanostructures and their application in photocatalytic technology for phasing out priority pollutants

Arshpreet Kaur<sup>1</sup> · Vidhi Suresh Mehta<sup>1</sup> · Gagandeep Kaur<sup>1</sup> · Dhiraj Sud<sup>1</sup>

Received: 31 October 2022 / Accepted: 6 January 2023 / Published online: 16 January 2023  
© The Author(s), under exclusive licence to Springer-Verlag GmbH Germany, part of Springer Nature 2023

## Abstract

Zinc oxide (ZnO) nanostructures have been successfully synthesized via template-assisted and template-free route using three different synthetic methods, i.e., sonochemical, mechanochemical, and hydrothermal. Biopolymer xanthan gum (XG) served as sacrificial template for ZnO synthesis as provided the surface for the growth of nanostructures in a controlled manner. The employment of multifarious synthetic techniques resulted in fabrication of ZnO nanoparticles with diverse morphologies such as needle shaped, hexagonal, and spherical particles. Further, the template-assisted protocols generated thermally stable highly crystalline nanostructures along with high surface area, larger pore size, and low band gap energies in contrast to template-free protocol. The structural and other physicochemical studies were manifested by XRD, N<sub>2</sub> adsorption desorption, FESEM, TGA, and UV–Vis spectral analysis. The template-assisted ZnO nanostructures were explored as a potential photocatalyst for the catalytic degradation of emerging pollutants, i.e., triclosan (TCS) and imidacloprid (IMD) under the exposure of UV light. The products formed during the photocatalytic reaction were monitored by UV–Vis spectroscopy and HPLC. The results obtained revealed the high catalytic efficiency of ZnO synthesized via template-assisted sonochemical method for TCS (99.60%) and IMD (96.09%) which is attributed to the high surface area and lower band gap energy of the catalyst. The high catalytic potential of the sonochemically synthesized ZnO also substantiated from the kinetic data as high-rate constant was obtained. Thus, the template-assisted protocols developed led to preparation of nanostructures having tailored properties for efficient photocatalysis and can rapidly degrade selected emerging contaminants such as personal care products and organophosphate pesticides. Hence, environment-friendly synthesized photocatalyst can be appropriately employed to wastewater treatment contaminated with emerging pollutants.

**Keywords** Xanthan gum · Template · Zinc oxide · Photocatalysis · Emerging pollutants

## Introduction

Nanotechnology is an emerging research arena which deals with the manipulation of matter at nanoscale and led to the fabrication of nanomaterials which possessed the multifaceted beneficial properties such as optical, catalytic, medicinal, electric, etc. (Khatoun et al. 2018). Generally, the transition metal oxide nanomaterials like TiO<sub>2</sub>, ZnO, MgO, CaO, etc., are considered promising candidates for plethora of applications such as in gas sensing (Maciak and Opilski 2007), photocatalysis (Rupa et al. 2018), and adsorption (Wang et al. 2019) and can also be utilized in solar cells (Masood et al. 2020), light emitting diodes (Schmidt et al. 2019), etc., owing to their significant crystallinity, variety of morphological features as functioning of nanomaterials basically rely upon the size, distribution, and morphology.

---

Responsible Editor: George Z. Kyzas

✉ Dhiraj Sud  
suddhiraj@yahoo.com

Arshpreet Kaur  
arshdhindsa225@gmail.com

Vidhi Suresh Mehta  
vidhimehta0330@gmail.com

Gagandeep Kaur  
gagangill2410@gmail.com

<sup>1</sup> Department of Chemistry, Sant Longowal Institute of Engineering and Technology, Deemed to Be University, Longowal 148106, Sangrur, India

Thus, to obtain the tailored properties for targeted application, there may be obligation of control over shape and size of the nanomaterial which can be accomplished with the usage of diverse stabilizers, reducing agents, templating agents, and by varying the synthesis methodologies (Luo et al. 2018).

There are several greener and conventional protocols which includes the template-assisted and template-free synthetic strategies that have been utilized for the metal oxide nanoparticle synthesis (Kaur et al. 2022a, b). However, the template-assisted greener synthetic approaches received a considerable interest to the researchers and this synthetic route is pocket friendly and economically safe as evades the use of organic solvents, surfactants, hazardous chemicals, etc. (Braun et al. 2005). Among the certain greener approaches, sonochemical (Amulya et al. 2020 and Singh et al. 2019a, b), hydrothermal (Zhang et al. 2019 and Suthakaran et al. 2020), and mechanochemical (Otis et al. 2021a, b and Pineda et al. 2018) are widely explored for the fabrication of metal oxide nanostructures having variety of morphological characteristics which in turn affects the physical and chemical properties of the material and accordingly can be employed for the targeted application.

The template-assisted synthesis carried out via top-down or bottom-up approach is an expedient strategy for fabrication of metal oxides due to the easy handling, unresponsiveness toward synthesis conditions, and resulted in the well-ordered morphological structures along with the high crystallinity and particle size in the nanodimensions (Takahashi et al. 2004). There are different template materials such as biopolymers (Nidhin et al. 2008), zeolites (Singh et al. 2019a, b), surfactants (Wang et al. 2002), ionic liquids (Zhou et al. 2004), anodic alumina membranes (Wu et al. 2004), etc., that have been employed for the synthesis of various metal oxide nanostructures. Biopolymeric materials such as chitosan (Nidhin et al. 2008), xanthan gum (Kaur et al. 2022a, b), calcium alginate (Kimling and Caruso 2012), dextran (Rafi et al. 2014), etc., seeks a massive consideration as a template due to their renewable, cheap, abundant, and non-toxic nature. In addition, the abundant functional moieties present onto polymeric backbone provides the active sites for the growth of nanostructured materials (Son et al. 2019).

Xanthan gum (XG) is a high molecular weight and double helical structured biopolymer widely explored for broad application spectrum, viz., chemical sensing (Kaur et al. 2020), waste water treatment (Kaur et al. 2022a, b), and pharmaceuticals (Li et al. 2019b) due to its biodegradable, biocompatible, non-toxic, highly viscous, and thermally stable nature. In addition, xanthan gum served as a template for the synthesis of metal oxide nanostructures owing to the presence of different functional moieties that are primary and secondary hydroxyl group, carboxyl group, and ester

group which resulted in the growth of nanostructures in a controlled manner (Kaur et al. 2022a, b). Herein, we report the exo-polysaccharide xanthan gum as a templating agent for the synthesis of nanostructured ZnO and the synthesis was carried out via three different greener protocols, i.e., sonochemical, mechanochemical, and hydrothermal. The impacts of template-free and template-assisted greener routes on the crystallinity, morphology, particle size, surface area, and photophysical properties of nanosized ZnO have been scrutinized.

Currently, the photocatalytic degradation process using materials having tremendous semiconductor properties has engrossed more significance toward the environmental remediation (Gusain et al. 2019 and Hayati et al. 2021). However, ZnO possessed the commendable semiconductor properties with wide band gap and high excitation binding energy (Samadi et al. 2019). ZnO is a highly resistant and durable material with low toxicity, economic viability, and easy availability. Owing to the high electron mobility and greater light harvesting capacity, ZnO is preferably employed in photocatalysis (Vaiano et al. 2018). In the present study, nanosized ZnO have been employed as catalyst for the photodegradation of emerging contaminants as the day-by-day contamination in water bodies by emerging pollutants has raised a concern in water quality standards. Moreover, the high concentration of these materials led to the worsening of surface and ground water, thereby causing a threat to environment as well as human health and, thus, their detection, analysis, and treatment became intricated and challenging. Materials that fall under emerging contaminants includes the pharmaceuticals, personal care products, pesticides, flame retardants, plasticizers, surfactants, etc. (Khan et al. 2019).

The occurrence and abolishing of personal care products and pesticides from the environment are a current hot-spot. The high consumption and uncontrolled discharge of these contaminants resulted in the microgram to nanogram concentration in surface water (Velempini et al. 2021 and Sabaghnia et al. 2019). The highly persistence nature of personal care products in the environment led to the transformation into highly toxic dioxins and chlorinated phenols, and many countries including Brazil have codification for their control through the CONAMA resolutions (National Council of the Environment) (Solá-Gutiérrez et al. 2020). Further, the excessive use of pesticides in agriculture boosted the food production by controlling the several pests but correspondingly resulted in the severe soil as well as ground water pollution (Mostafa et al. 2021 and Taghavi et al. 2022). According to the annual survey, there is a 2.5 million ton usage of pesticide all over the world; however, only 0.1% pesticides applied to the crop for better production of food and the remaining amount (99.9%) of pesticide disseminated through air, water, and soil, thereby causing the pollution (Bano et al. 2021 and Radwan et al. 2020). Thus,

pesticides are one of the most commonly detected pollutants in surface and ground waters of agricultural areas, and due to the unwise use of pesticides, the situation will become more aggravated with the passage of time (Natsathaporn et al. 2020 and Mansor et al. 2022). So, the removal of these hazardous contaminants from environment is highly needed. However, exclusion of such pollutants via traditional methods is very hard and could be photocatalytically degraded by employing suitable catalyst (Himanshi et al. 2022). Thus, herein we have chosen two model compounds, i.e., TCS which is an antibacterial agent widely used in personal care products and an organophosphate pesticide, i.e., IMD for the evaluation of photocatalytic potential of synthesized ZnO nanostructures.

## Materials and methods

XG and zinc acetate were purchased from Sigma Aldrich, India. Ammonia solution used during synthesis of the photocatalyst was received from SD Fine-Chem, Limited. For photocatalytic reactions, triclosan of USP grade was obtained from Dev Impex (Bileshwarpura, Chhatral, New Gujarat, India), and imidacloprid and chlorpyrifos of 99% purity was provided from Crops Chemical Limited, Kotakpura, Punjab. All the solutions required for photocatalyst

synthesis and analyte solutions were prepared using deionized water.

## Template-assisted synthesis of ZnO nanoparticles

The template-assisted synthesis of ZnO nanoparticles was carried out using exo-polysaccharide XG as a template via three different greener protocols, i.e., sonochemical, mechanochemical, and hydrothermal method as shown in Fig. 1. In a typical procedure, 0.1 M zinc acetate solution and 0.25% XG solution were prepared in deionized water and mixed in the volume ratio 1:1. The mixture became viscous owing to the XG and inorganic precursor interactions. The mixture was stirred at 400 rpm and at room temperature. After 30 min stirring, 6.5 mL of 10%  $\text{NH}_4\text{OH}$  was added to the reaction mixture which resulted in the formation of white colored precipitates. Then, the reaction mixture was stirred for an hour.

For sonochemical synthesis, the reaction mixture was kept in probe sonicator and the ultrasonic waves of 40 kHz were exposed for 30 min at 45 °C.

In hydrothermal synthesis, the reaction mixture was subjected in Teflon-lined steel autoclave which was kept in muffle furnace at 100 °C to carry out the reaction for 9 h.

For mechanochemical synthesis, the reaction mixture was firstly filtered and dried in hot air oven. Then, the

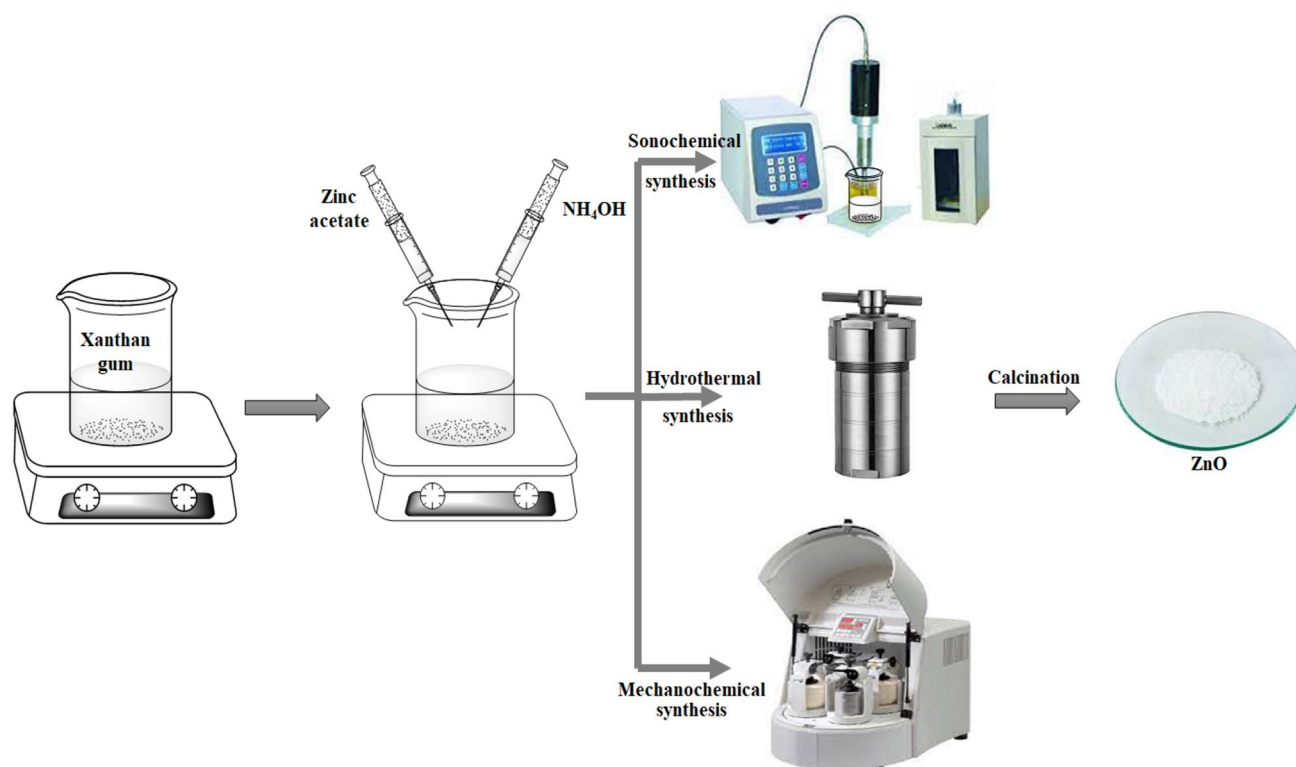


Fig. 1 Schematic overview of synthesis of ZnO

white-colored powder and grinding balls of 1 mm diameter were placed in a 100-mL cup with steel casting with a powder/ball mass ratio of 1:100. The cups were sealed and kept in planetary ball mill to perform the milling cycles at 400 rpm. The cycles were performed for 1 min followed by a 10 min pause before the next run. In this manner, the sample was subjected for 10 cycles (Otis et al. 2021a, b).

Upon the completion of reaction using three techniques, the resultant mixture was filtered and washed 3–4 times with deionized water and ethanol mixture to remove the impurities. Then, the sample was dried in hot air oven for 4 h at 70 °C. Further, the sample was calcinated at 300 °C for 2 h which may lead to the removal of template traces left during the washings of sample; thus, pure ZnO was obtained. The template-assisted ZnO fabricated using sonochemical, hydrothermal, and mechanochemical methods are referred as ZnO-TS, ZnO-TH, and ZnO-TM, respectively. Similarly, the synthesis of ZnO was carried out via template-free strategy, i.e., without aid of XG using sonochemical, hydrothermal, and mechanochemical methods, and these synthesized ZnO samples were designated as ZnO-S, ZnO-H, and ZnO-M, respectively, and characterized by various techniques.

### Photocatalytic activity

The photocatalytic performance of ZnO nanoparticles synthesized using three different techniques via template-assisted route for the degradation of priority pollutant TCS and organophosphate pesticide IMD was tested under UV light. For the photo-catalytically degradation experiment, 50 ppm solution of both analytes was taken in two different flasks containing 100 mg of catalyst and the reaction flasks were kept in dark to achieve the adsorption–desorption equilibrium. Further, the photo-degradation reaction was proceeded in a self-designed photoreactor equipped with assembly of UV light tubes for photocatalytic degradation (irradiation of model compound) experiments. In a photochemical chamber, the reaction mixtures were stirred at 300 rpm, oxygenated with air flux and exposed to UV light and continuously stirred. Thereafter, the aliquots of analyte (3 mL) were taken after specified time intervals using syringe and placed in the quartz cuvette of 1 cm length by passing through the syringe filter. The UV spectra was recorded using UV–visible spectrophotometer and noted the intensities of analytes corresponding to their respective  $\lambda_{\max}$ . The degradation rate of TCS and IMD was studied in terms of change in absorbance as a function of time.

The percentage degradation of the organic pollutant TCS and IMD was calculated using equation (Rodrigues et al. 2019)

$$\text{Percentage Degradation} = \frac{(A_0 - A)}{A_0} \times 100$$

where  $A_0$  is the initial concentration of the organic pollutant and  $A$  is the concentration of organic pollutant after irradiation under different light sources.

The kinetics of the degradation process was evaluated using the following equation (Lin et al. 2018):

$$\ln \frac{C_0}{C_t} = kt$$

where  $C_0$  and  $C_t$  are the concentrations at time  $t=0$  and  $t=t$  and  $k$  is the pseudo-first-order rate constant.

### Characterization

The synthesized ZnO nanoparticles were characterized by various physico-chemical techniques. X-ray diffraction (XRD) pattern of ZnO was recorded on X-ray diffractometer D8 Advance Bruker for  $2\theta$  value of 25°–80° with a scan speed of 10°/min. The surface morphology of the synthesized template-free and template-assisted ZnO was characterized by FE-SEM analysis (JSM-7610Plus JEOL) at an accelerating voltage of 10–15 kV. The vibrational spectral analysis was performed using Spectrum RX-IFTIR, Perkin Elmer, over the range from 400 to 4000  $\text{cm}^{-1}$ . The thermal stability of ZnO nanostructures was evaluated from thermogravimetric analysis (TGA) over the temperature range 50–700 °C with 10 °C/min heating rate. The  $\text{N}_2$  adsorption/desorption isotherm and pore size distribution were analyzed by performing BET surface area analysis on a Quantachrome Autosorbe 1Q-MP-AG (2 Stat.) Viton instrument. Further, the band gap energy evaluation has been carried out by performing UV–Vis spectral analysis using UV-1800, Shimadzu spectrophotometer. The photocatalytic degradation studies have also been monitored by recording the absorption spectra using UV–Vis spectrophotometer. The concentration of triclosan, imidacloprid, and their by-products was followed by high-performance liquid chromatography (HPLC) using a Hewlett-Packard liquid chromatography system (HP1050) equipped with photodiode array detector and an automatic injector. The experiments were performed by UV detection at 280 nm. The flow rate was 1.0  $\text{mL min}^{-1}$  and the injected volume was 10  $\mu\text{L}$ . The elution was accomplished with methanol and phosphate (pH=3) (72:28 by volume).

### Results and discussion

The schematic representation of the fabrication and growth of the nanostructured ZnO using different techniques is presented in Fig. 2. The synthesis has been carried out by

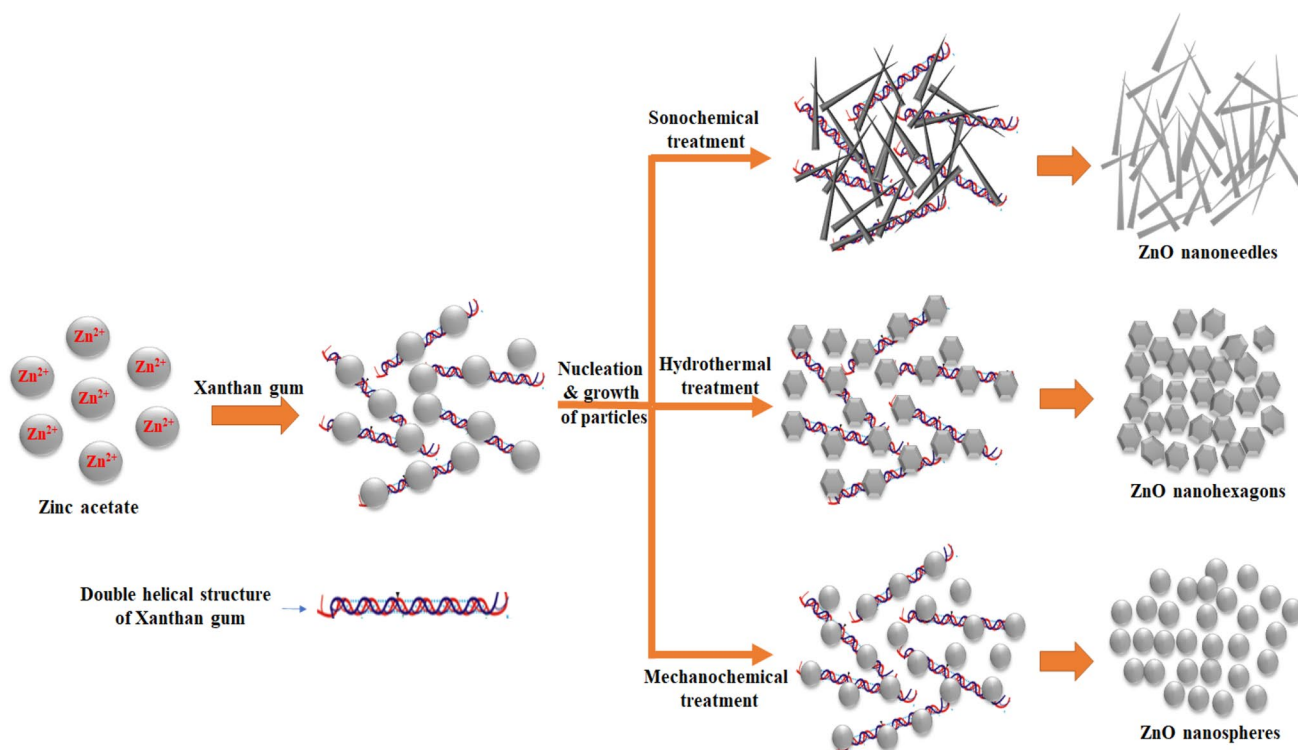


**Fig. 2** Fabrication and growth of template-assisted ZnO nanostructures

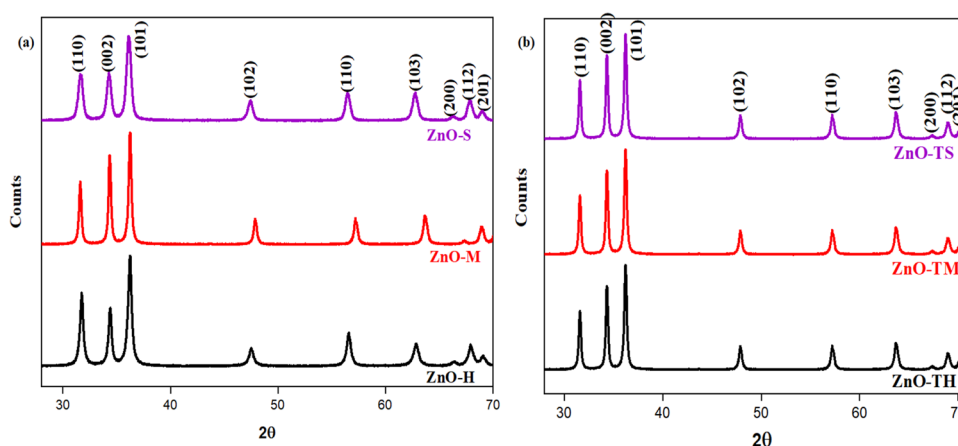
template-assisted developed protocols as well as with template-free methods. The template-assisted hydrothermal, sonochemical, and mechanochemical method led to the formation of highly crystallined hexagonal, needle-shaped, and spherical structures, respectively, whereas rod-shaped and agglomerated spherical ZnO particles were obtained using template-free strategy. The double helical structural surface of XG being highly rich in oxygen functionalities such as  $-OH$  and  $C=O$  binds the metal ions onto the surface and provides the nucleation sites for the growth of nanostructures in a controlled manner onto template surface. During the reaction time, the growing nanostructures were densified

and crosslinked in a successive manner during the hydrothermal, sonochemical, and mechanochemical treatments that eventually resulted in free standing porous and nanostructured ZnO after the removal of the XG template.

**Crystal structure analysis**

XRD analysis elucidates the formation of highly crystalline ZnO nanoparticles by template-assisted and template-free methodology using different techniques. XRD pattern of all ZnO samples (Fig. 3) showed the diffraction peaks at 31.777, 34.424, 36.2, 47.548, 56.588, 62.890, 66.399, 67.918, and

**Fig. 3** XRD pattern of **a** template-free and **b** template-assisted ZnO nanostructures



69.129 corresponding to (1 0 0), (0 0 2), (1 0 1), (1 0 2), (1 1 0), (1 0 3), (2 0 0), (1 1 2), and (2 0 1) crystal planes of ZnO. All the diffractions peaks perfectly coincide with the JCPDS card 01–071–6424 which confirmed the formation of pure ZnO having wurtzite hexagonal crystal structure with P63mc (1 8 6) space group, and volume of unit cell 47.58. The average crystallite of all the samples was calculated using Debye Scherrer equation (1),

$$D = 0.9\lambda / \beta \cos\theta$$

where  $D$  represents the Average particle size,  $B$  is the full width at half maxima (FWHM),  $\theta$  represents the Bragg's angle, and  $\lambda$  is the wavelength of CuK $\alpha$  radiations.

The presence of crystallographic defect or irregularity in the crystal lattice is known as dislocation density which rely upon the length of dislocation lines per unit volume of the crystal. The extent of dislocation density influenced the properties of the crystal (Pachiyappan et al. 2020). The dependency of hardness of crystal upon the dislocation density extent exemplifies the influence of dislocation density on the properties of crystal. Owing to the crystal imperfections, some strain develops in the crystal, known as lattice strain. The lattice strain and dislocation density for all the samples have been calculated using equations (Satdeve et al. 2019)

$$\text{Dislocation density} = 1/D^2$$

$$\text{Lattice strain} = \beta/4 \tan \theta$$

Thus, the data depicts the fabrication of pure and highly crystallized ZnO having dimensions in nanorange via template-assisted and template-free methodology using different techniques. However, ZnO-TS, ZnO-TH, and ZnO-TM samples, i.e., ZnO prepared via template-assisted methodology, possessed the smaller crystallite size as compared to ZnO-S, ZnO-H, and ZnO-M samples that were synthesized via template-free route. The slight variation in average crystallite was observed by varying the synthesis technique which further effects the dislocation density and strain of the lattice crystal which are shown in Table 1. The lowest average crystallite size was obtained for ZnO-TS which amended the surface properties and thereby improved the photocatalytic efficiency of catalyst.

### Vibrational analysis

The vibrational spectra of ZnO synthesized by template-assisted and template-free route using different methods (Fig. 4) confirmed the successful synthesis of ZnO by analyzing the presence of metal-oxide bond in the compound. The FTIR spectra of all the compounds showing the characteristic peaks at 3435 cm<sup>-1</sup> attributed to the stretching vibrations, and peaks at 1387 cm<sup>-1</sup> and 1665 cm<sup>-1</sup> correspond to the bending vibrations

**Table 1** Average crystallite size, dislocation density, and lattice strain of synthesized ZnO nanostructures

| Sample | Average crystallite size ( $D$ ) (nm) | Dislocation density | Lattice strain |
|--------|---------------------------------------|---------------------|----------------|
| ZnO-TS | 11.76317622                           | 0.005065472         | 0.008984324    |
| ZnO-TH | 12.23152556                           | 0.004512384         | 0.007846318    |
| ZnO-TM | 14.27634222                           | 0.004236582         | 0.006002440    |
| ZnO-S  | 21.23152556                           | 0.002349093         | 0.003942354    |
| ZnO-H  | 28.5486155                            | 0.001929513         | 0.004111286    |
| ZnO-M  | 39.5581156                            | 0.001439093         | 0.004526782    |

of –OH group of the surface adsorbed water from atmospheric moisture. The peak corresponding to 890 cm<sup>-1</sup> represents the formation of tetrahedrally coordinated Zn (Li et al. 2019a). Further, the intense peak at 497 cm<sup>-1</sup> which is the characteristic peak for Zn–O bond demonstrated the successful ZnO fabrication by template-assisted route using different techniques. The vibrational spectra of ZnO-S, ZnO-M, and ZnO-H showed the presence of additional peaks at 2900 cm<sup>-1</sup> which corresponds to –CH stretch due to the presence of precursor residue. Hence, results demonstrated that the template-assisted strategy led to the formation of pure ZnO.

### Thermal analysis

The thermal stability of the nanostructured ZnO prepared by different techniques has been evaluated by TGA analysis. The thermo-graphs of ZnO-TS, ZnO-TM, and ZnO-TH (shown in Fig. 5) revealed the high thermal stability of samples as only 1%, 1.4%, and 2% weight losses, respectively, happened at 600 °C, which may be attributed to the loss of water molecules that were physically adsorbed onto surface of ZnO from atmosphere (Alomair and Mohamed 2018). Thus, above 98% of synthesized ZnO was existing even after heating up to 600 °C. However, ZnO-S, ZnO-M, and ZnO-H showed the 10%, 12%, and 15% weight losses, respectively, up to 600 °C. Thus, in contrast to ZnO synthesized via template-free route, the template-assisted strategy resulted in the pure and highly thermal stable ZnO nanostructures which may attributed to the double helical structure of negatively charged XG and the presence of hydroxyl and carboxylic hydrophilic functional moieties which tends to form a steric barrier and ultimately stabilize the surface. Convincingly, ZnO synthesized via template-assisted ultrasonication method possesses the highest thermal stability among all the synthesized samples.

### UV–Vis absorption spectra

The UV–Vis absorption spectra of ZnO synthesized via different strategies were recorded in the range of 190 to 800 nm.

**Fig. 4** Vibrational spectra of **a** template-free and **b** template-assisted ZnO nanostructures

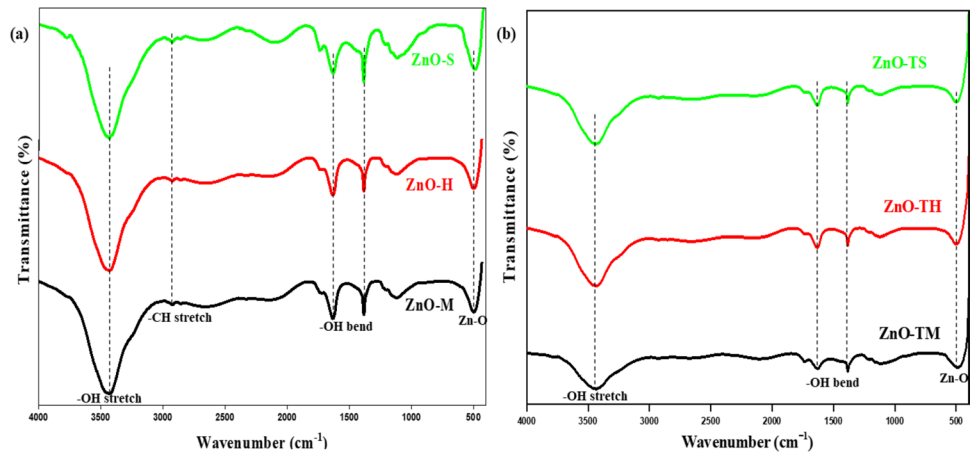
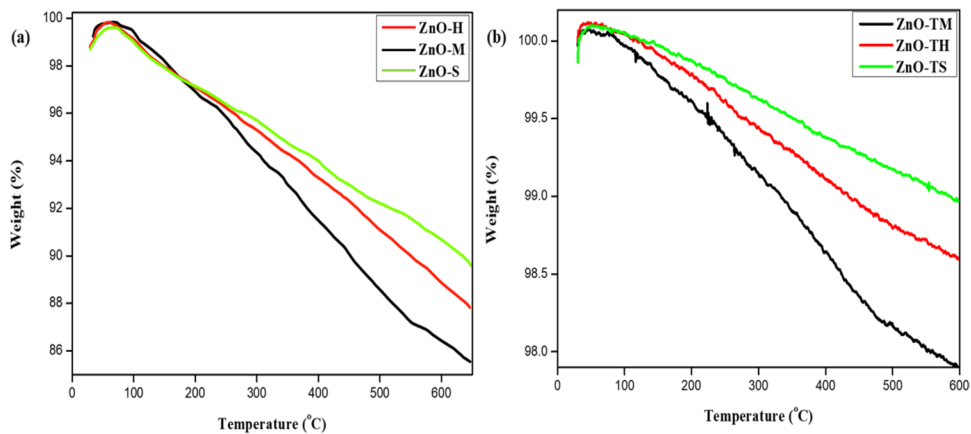


**Fig. 5** TGA of **a** template-free and **b** template-assisted ZnO nanostructures



The single and broad intense absorption spectra of ZnO synthesized usually attributed to charge transfer from the valence band (mainly formed by 2p orbitals of the oxide anions) to the conduction band (mainly formed by 3d orbitals of the Zn<sup>2+</sup> cations) (Singha and Patra 2020). ZnO-H and ZnO-TH showed the absorption edges corresponding to 370.0 nm and 372.7 nm wavelengths, while bathochromic shift was observed for ZnO-M, ZnO-TM, ZnO-S, and ZnO-TS as absorption peaks were recorded at 371.9 nm, 373.1 nm, 372.7 nm, and 370.0 nm, respectively (Fig. 6).

The excess absorbance for template-assisted ZnO ascribed to the creation of more vacant anionic sites on the surface by a template which enhanced the exposure for the valence band electrons and thus high charge transfer density from valence band to conduction band. These shifts toward the higher energy wavelength of light imply band gap narrowing in ZnO-TS followed by ZnO-TM, ZnO-TH, ZnO-S, ZnO-M, and ZnO-H as confirmed by the analysis of the spectroscopic data via Tauc plots using the equation

$$(\alpha h\nu)^2 = C' (h\nu - E_g)$$

where

- $\alpha$  absorption coefficient of the material
- $\lambda$  wavelength (nm)
- $C'$  Planck's constant
- $h$  proportionality constant
- $\nu$  frequency of light
- $E_g$  band gap energy

The Tauc's graphs were plotted between  $(\alpha h\nu)^2$  vs.  $h\nu$  for ZnO-TS, ZnO-TM and ZnO-TH, ZnO-S, ZnO-M, and ZnO-H (Fig. 7). The meeting of extrapolation of linear portion of curve plotted between  $(\alpha h\nu)^2$  and  $h\nu$  to the abscissa gave the values of band gap energies which are shown in Table 2. Thus, it was perceived that the employment of different synthetic approaches for preparation of ZnO nanoparticles effects the band gap energy, thereby affecting the photocatalytic properties of ZnO as photocatalytic efficiency of compound directly depends upon the band gap energy.

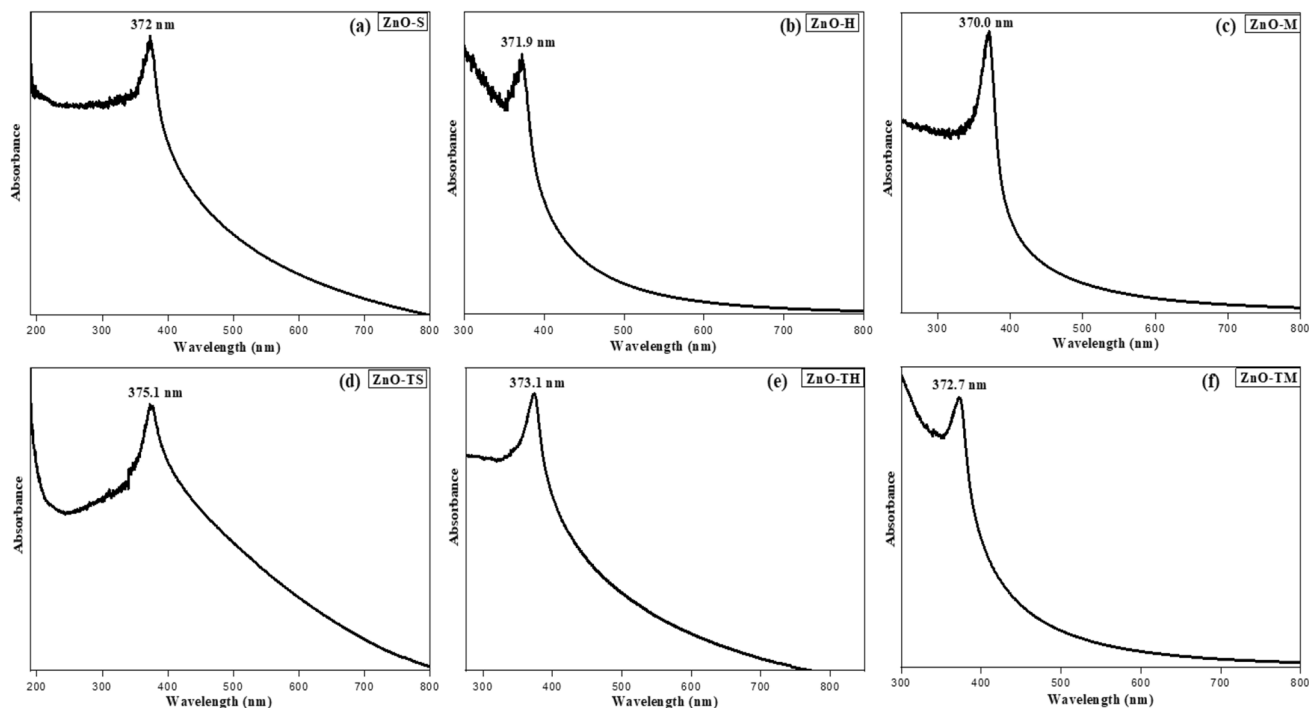


**Fig. 6** UV-Vis absorption spectra of **a–c** template-free and **d–f** template-assisted ZnO nanostructures

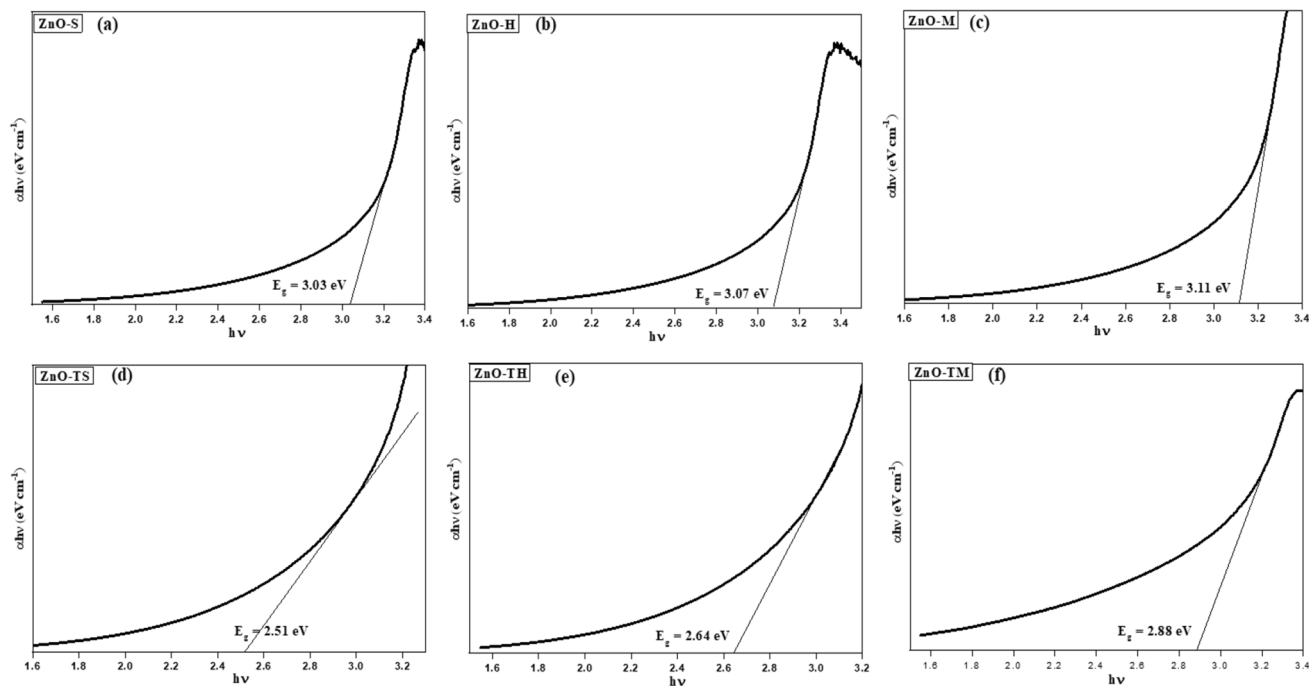


**Fig. 7** Tauc's plot for **a–c** template-free and **d–f** template-assisted ZnO nanostructures

### Morphological and EDS analysis

The surface morphologies and elemental composition of ZnO-TS, ZnO-TH and ZnO-TM, ZnO-S, ZnO-H, and ZnO-M were examined by field emission scanning

electron microscope as shown in Fig. 8. FESEM analysis revealed the significant impact of synthesis protocols on the morphology of ZnO as different nanostructures were obtained depending upon the synthetic method. The template-free sonochemical synthetic strategy (ZnO-S



**Table 2** Absorption peaks corresponding to maximum wavelength and band gap energies of synthesized ZnO

| Photocatalyst | $\lambda_{\max}$ (nm) | Band gap (eV) |
|---------------|-----------------------|---------------|
| ZnO-TS        | 375.1                 | 2.51          |
| ZnO-TM        | 373.1                 | 2.64          |
| ZnO-TH        | 372.7                 | 2.88          |
| ZnO-S         | 372.0                 | 3.03          |
| ZnO-M         | 371.9                 | 3.07          |
| ZnO-H         | 370.0                 | 3.11          |

sample) resulted in the synthesis of rod-like morphology of ZnO-S sample, whereas the template-assisted sonochemical synthesis of ZnO-TS led to the formation of elongated needle-shaped particles. The template-assisted and template-free hydrothermal (ZnO-TH and ZnO-H) route furnished the highly crystalline hexagonal and worm-like morphology, respectively. However, the mechanochemical approach led to the formation of agglomerated spherical particles via template-free approach while uniform and non-agglomerated spherical morphology of ZnO nanoparticles was obtained via template-assisted approach. Thus, the template-assisted synthetic protocol led to the formation of nanoparticles possessing the highly uniformed and crystalline morphological characteristics. The average particle size of all the synthesized ZnO samples was evaluated from particle size distribution curve (Fig. 8) using ImageJ software. Further, the results obtained from the EDS suggested that the ZnO powder has good purity as no peak for other element was observed.

DLS (dynamic light scattering) analyses of ZnO nanostructures synthesized by template-assisted and template-free strategies are shown in Fig. 9, suggesting the average particle size distribution in the range of 23 to 50 nm and 12 to 37 nm for template-free and template-assisted ZnO, respectively. Further, the polydispersity indexes for ZnO-S, ZnO-H, and ZnO-M were found to be 0.891, 0.916, and 0.992, whereas 0.524, 0.601, and 0.694 were observed for the ZnO-TS, ZnO-TH, and ZnO-TM nanoparticles, respectively, which revealed the high uniformity in template-assisted ZnO nanostructures as compared to template freely synthesized ZnO. Thus, the DLS data confirmed the variation in size as well as homogeneity of ZnO NPs by changing the synthetic protocol.

### Surface area analysis

The catalytic potential of catalyst directly depends upon the porous nature and availability of surface area for the analytes to make contact with the catalysts. In present study,  $N_2$

adsorption–desorption and BJH pore size distribution analysis (inset) of ZnO-S, ZnO-H, and ZnO-M synthesized via template-assisted and template-free route were carried out as shown in Fig. 10. It has been observed that ZnO-TS sample possessing nano-needle-like morphology exhibited the high surface area, pore volume, and pore diameter as compared to other synthesized catalysts (compiled in Table 3) which in turn resulted in the high catalytic efficiency of the catalyst. Interestingly, it has been observed that the BET surface area of template-assisted ZnO is significantly higher than the ZnO synthesized via template-free route. The results pinpoint the tremendous effect of XG (template) on the enhancement of surface area and porosity of ZnO by providing controlled nucleation growth of nanostructures onto double helically structured template surface. In addition, the surface area of commercially available ZnO was reported to be 3.23 m<sup>2</sup>/g which was approximately 6 times lower than that of synthesized ZnO via template-assisted and template-free methodologies.

Conclusively, it has been observed that the ZnO nanoparticles synthesized via template-assisted protocol owned the high crystallinity, small crystallite size, as well as significant surface area. The high surface area of the synthesized material improves the photocatalytic properties of the material by making a larger contact area with the target material, and thus absorbed the higher amount of substrate molecules. In addition, the lower band gap energies of template-assisted nanostructures ZnO made them accessible for better catalytic performance under different light conditions. Thus, photocatalytic efficiencies of template-assisted ZnO samples, i.e., ZnO-S, ZnO-H, and ZnO-M, have been evaluated for the degradation of TCS and IMD.

### Evaluation of photocatalytic performance of template-assisted ZnO nanostructures

The photocatalytic performance of ZnO nanostructures was appraised by the degradation of TCS and IMD in aqueous solution at 50 ppm under UV light. Priorly, the direct photolysis of TCS and IMD has been carried out in the absence of catalyst and results displayed only 4.02% degradation of TCS while 3.81% degradation of IMD have been observed in 10 days under the exposure of UV light. The results revealed that decomposition of TCS and IMD is extremely slow in the absence of catalyst. Further, the photocatalytic degradation studies of TCS and IMD have been performed employing ZnO-TS, ZnO-TH, and ZnO-TM as a photocatalyst and the degradation was monitored via UV–Vis spectral analysis. To evade the involvement of adsorption, the solution of TCS and IMD with the photocatalyst was kept in the dark for 30 min to achieve adsorption equilibrium and results demonstrated 6.70% and 5.92% adsorption efficiency for TCS and

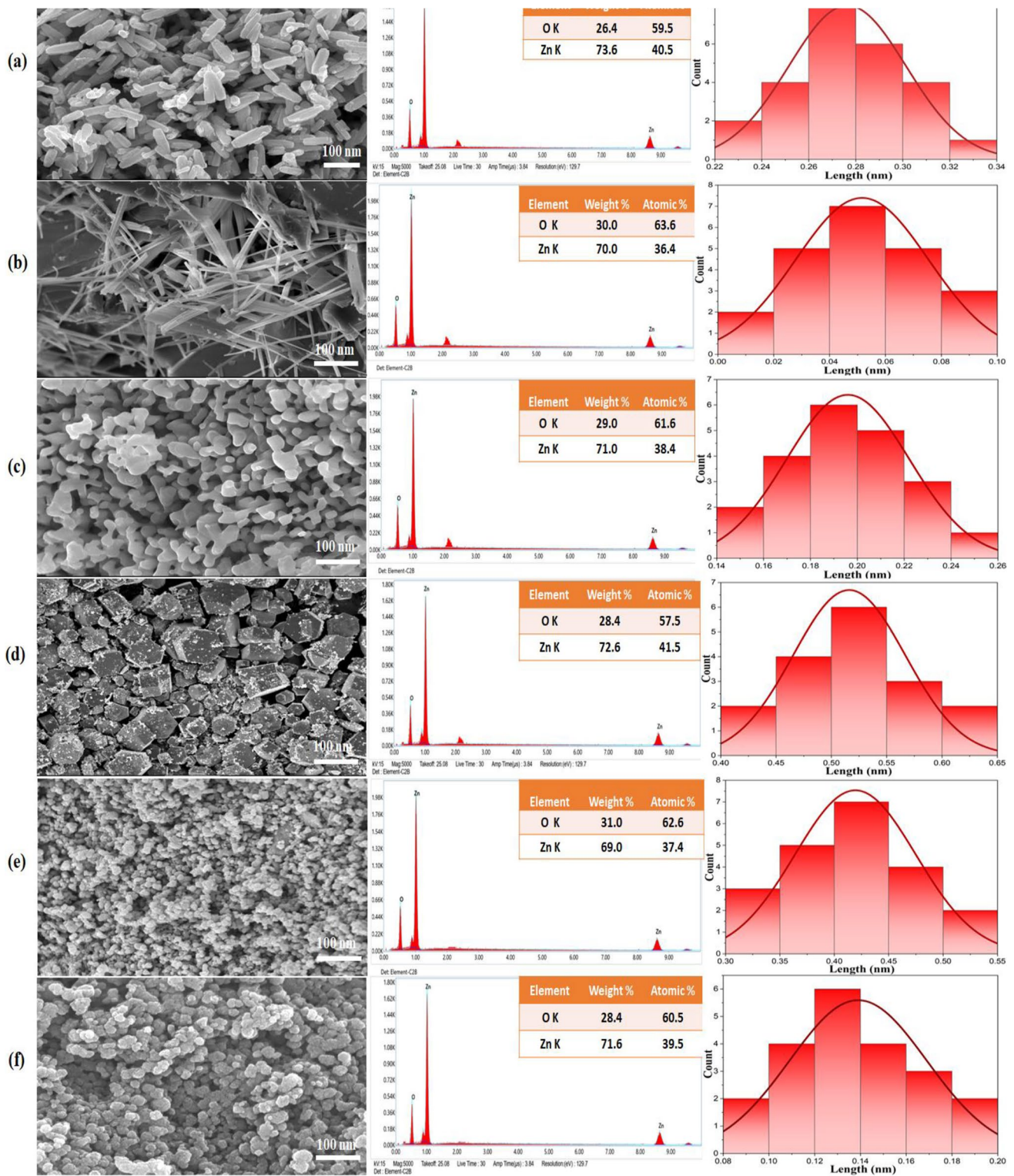


**Fig. 8** FESEM images, EDS, and particle size distribution curve of **a** ZnO-S, **b** ZnO-TS, **c** ZnO-H, **d** ZnO-TH, **e** ZnO-M, and **f** ZnO-TM nanostructures

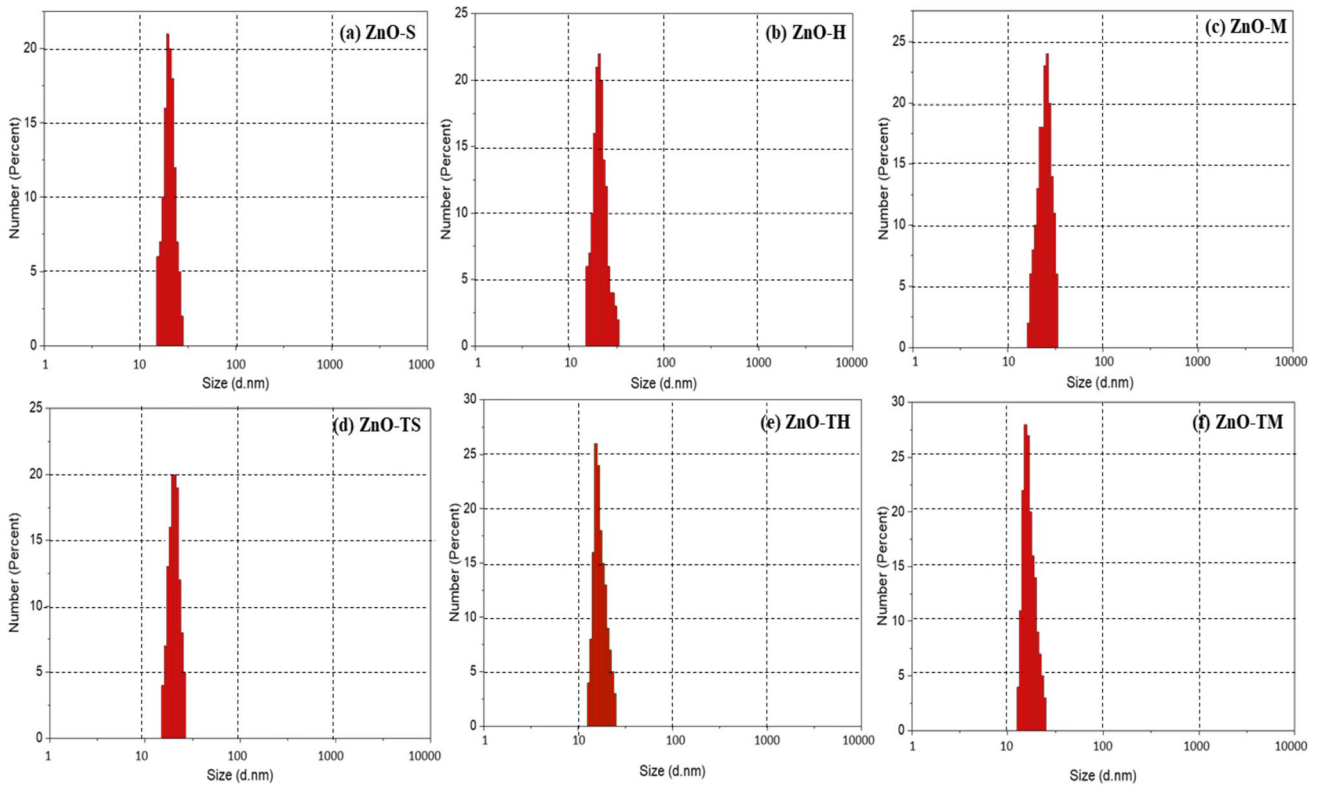


Fig. 9 DLS analysis of a–c template-free and d–f template-assisted ZnO nanostructures

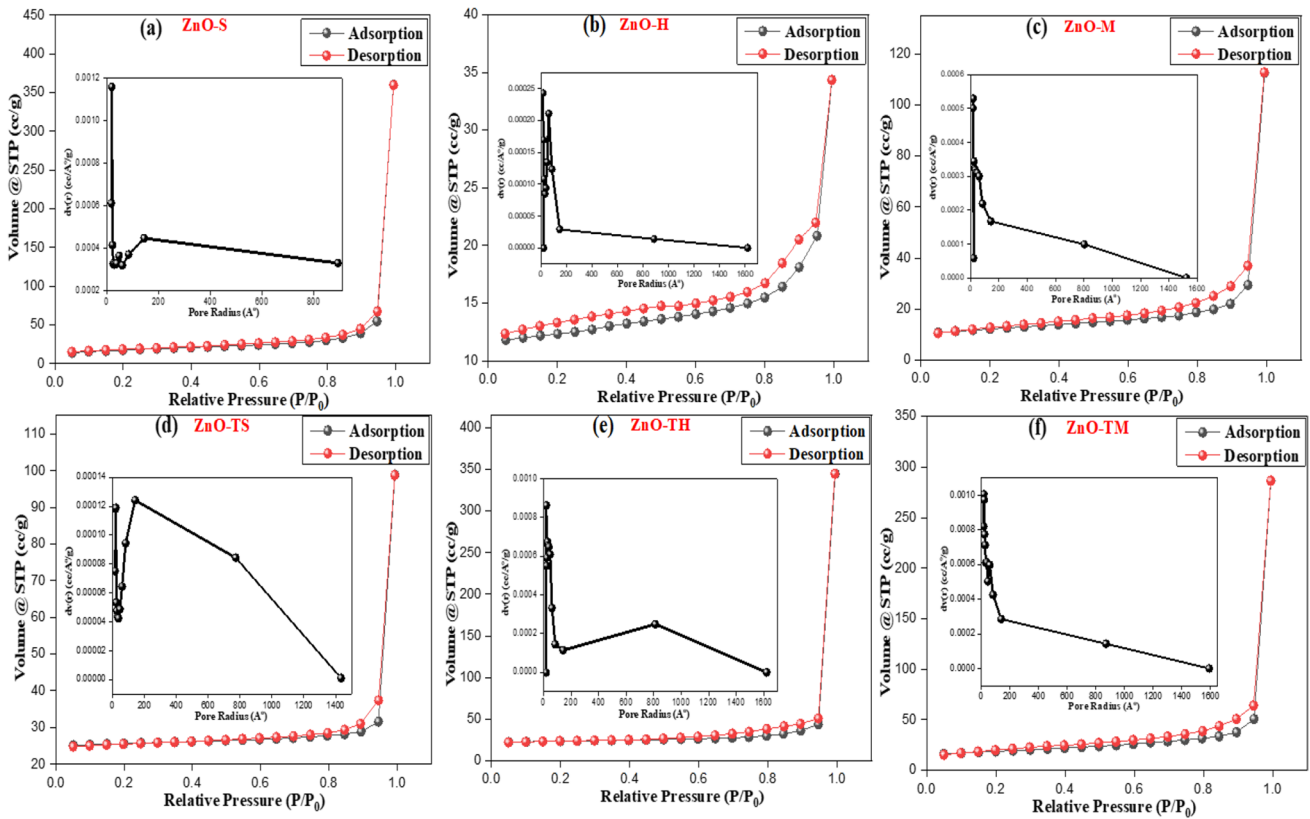
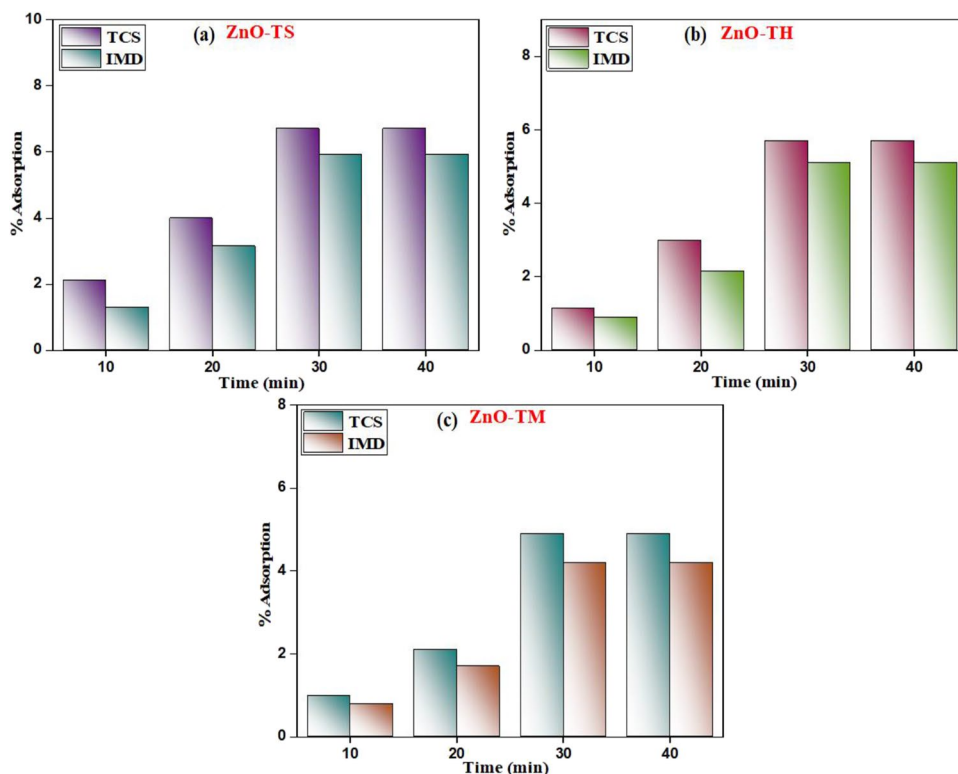


Fig. 10 N<sub>2</sub> adsorption/desorption and BJH pore size distribution curve (inset) of a–c template-free and d–f template-assisted ZnO nanostructures

**Table 3** Surface area, Langmuir surface area, pore radius, and pore volumes of template-assisted and template-free ZnO nanostructures

| Sample | BET surface area (m <sup>2</sup> g <sup>-1</sup> ) | Langmuir surface area (m <sup>2</sup> g <sup>-1</sup> ) | Pore radius (nm) | Pore volume (cm <sup>3</sup> g <sup>-1</sup> ) |
|--------|--|---|------------------|--|
| ZnO-S  | 54.19  | 106.38  | 1.912            | 0.394  |
| ZnO-H  | 45.67  | 95.56   | 1.707            | 0.152  |
| ZnO-M  | 39.42  | 79.16   | 1.419            | 0.116  |
| ZnO-TS | 105.68   | 215.91  | 6.406            | 0.981  |
| ZnO-TH | 94.93  | 189.38  | 6.043            | 0.587  |
| ZnO-TM | 82.16  | 163.29  | 2.902            | 0.354  |

**Fig. 11** Adsorption behavior of **a** ZnO-TS, **b** ZnO-TM, and **c** ZnO-TH toward TCS and IMD

IMD (Fig. 11), respectively. Subsequently, the suspension was placed in the photocatalytic chamber for irradiation.

### Effect of synthesis method of photocatalyst on photocatalytic degradation and kinetic study

The systematic investigation on the degradation process of TCS and IMD using template-assisted ZnO catalyst, i.e., ZnO-TS, ZnO-TM, and ZnO-TH, has been carried out along with the evaluation of kinetic parameters by performing contact time experiment under exposure of UV light. Primarily, the UV–Vis spectral analysis of TCS and IMD has been performed which showed the characteristic peak corresponding to 280 nm and 269 nm, respectively. Then, the aqueous solution of TCS and IMD was taken in different Erlenmeyer flasks and each flask contained a synthesized photocatalysts that has been irradiated

with UV light under constant stirring. The change in absorbance of the TCS and catalyst suspension was at  $\lambda = 280$  nm, and for IMD, the absorbance corresponding to  $\lambda = 269$  nm was recorded at a 5 min interval up to 50 min.

The ZnO-TS catalyst exhibited the maximum catalytic efficiency as it reached the 99.60% degradation of TCS after 30 min under UV light (Fig. 12(a,b)) and further continuity of light contact with the suspension resulted in no change in degradation efficiency of catalyst. Similarly, the catalyzed photolysis experiments for IMD degradation have been performed which showed the 96.09% degradation using ZnO-TS catalyst under UV light. However, ZnO-TH and ZnO-TM also exhibited the significant catalytic efficiency for TCS degradation when exposed to UV which is shown in Table 4. The photocatalytic efficiency of catalyst was significantly affected by various factors like

**Fig. 12** a, b Effect of different synthesis strategies of catalyst on photocatalytic degradation of TCS and IMD and c, d pseudo-first-order kinetic plot

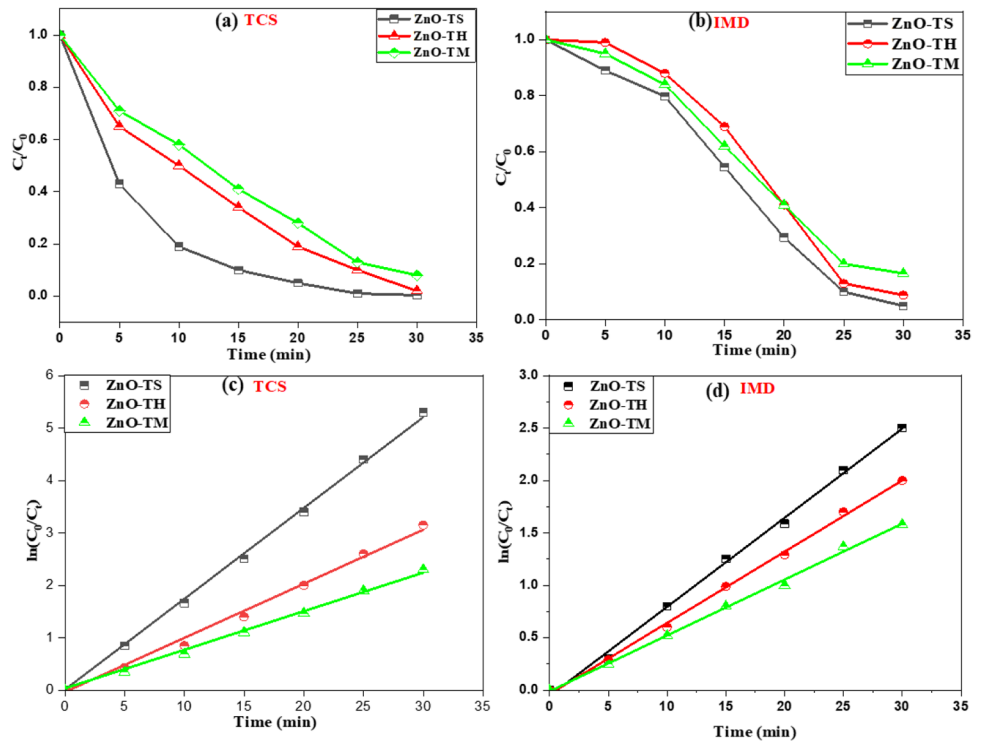


**Table 4** Represents the effect of synthesis method of catalyst on % degradation and rate constant

| Sample | Light source | Irradiation time (min) |     | Maximum degradation (%) |       | Pseudo-first-order rate constant (min <sup>-1</sup> ) |                | R <sup>2</sup> |        |
|--------|--------------|------------------------|-----|-------------------------|-------|---|----------------|----------------|--------|
|        |              | TCS                    | IMD | TCS                     | IMD   | TCS   | IMD            | TCS            | IMD    |
| ZnO-TS | UV           | 30                     | 30  | 99.60                   | 96.09 | 0.175 ± 0.0025  | 0.084 ± 0.0019 | 0.9963         | 0.9974 |
| ZnO-TH | UV           | 30                     | 30  | 96.64                   | 93.21 | 0.101 ± 0.006   | 0.067 ± 0.0013 | 0.9894         | 0.9981 |
| ZnO-TM | UV           | 30                     | 30  | 90.26                   | 87.30 | 0.078 ± 0.0002  | 0.053 ± 0.0012 | 0.9879         | 0.9971 |

crystallite size, surface area, and band gap energy of the catalyst. Owing to the smaller crystallite size, high surface area and low band gap energy of ZnO-TS photocatalyst in contrast to ZnO-TH and ZnO-TM govern the high catalytic efficiency of ZnO-S catalyst under UV light.

The kinetic studies for degradation of TSC and IMD were assessed and pseudo-first-order model was tested to evaluate the kinetics rate (Fig. 12(c,d)) for the degradation process using the ZnO nanoparticles under the exposure of UV light. The graph between  $C/C_0$  vs time was plotted for different catalysts used, and the rate of reaction was determined from the slope of the plot. The obtained pseudo-first-order degradation rates for ZnO-TS, ZnO-TM, and ZnO-TH and values of correlation factor are compiled in Table 4. As the high degradation rate using ZnO-TS catalyst was observed, further experimentation on photocatalytic efficiency was restricted to ZnO-TS as an efficient photocatalyst and impact of variables impacting the efficiency was investigated.

**Initial concentration**

The impact of initial concentrations of targeted material, i.e., TCS and IMD, on the photodegradation activity has been studied by varying the initial concentrations from 10 to 50 mg/L. Results on the comparison of % degradation of TCS and IMD using ZnO-TS catalyst under the exposure of UV are shown in Fig. 13. With the increase in initial concentration from 10 to 40 mg/L, the significant decreases of % degradation of TCS and IMD are from 99.60, 96.09% to 49.73, 47.92%, respectively. Further increment in concentration led to the negligible diminution of degradation efficiency. The degradation rates for photocatalytic reactions have also been evaluated and rate constants are shown in Table 5. The lowering of % degradation with increase in concentration of TCS and IMD may be attributed to the occupation of large number of active sites of photocatalyst by adsorption of analyte molecules, thus, resulting in the lower number of vacant or active sites for O<sub>2</sub> and OH adsorption,

**Fig. 13** a, b Effect of initial concentration of TCS and IMD on photocatalytic degradation and c, d pseudo-first-order kinetic plots

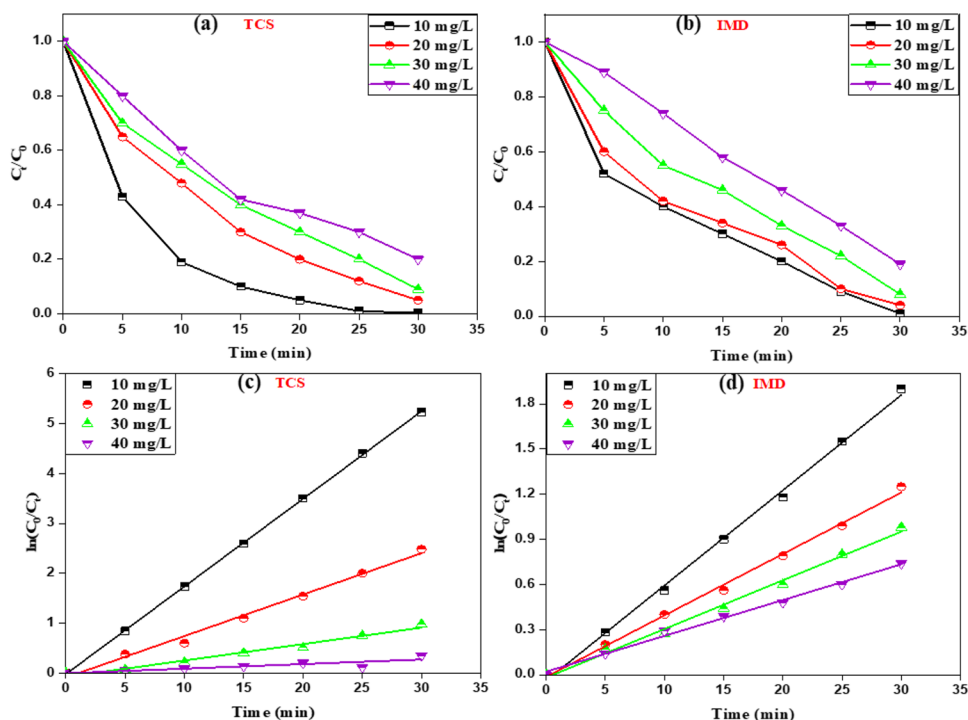


**Table 5** Represents the effect of initial concentration of TCS and IMD on rate constant

| Analyte | Conc. of analyte (mg/L) | Rate constant ( $\text{min}^{-1}$ ) | $R^2$  |
|---------|-------------------------|-------------------------------------|--------|
| TCS     | 10                      | $0.1755 \pm 0.0008$                 | 0.9998 |
|         | 20                      | $0.0830 \pm 0.0034$                 | 0.9915 |
|         | 30                      | $0.0328 \pm 0.0022$                 | 0.9764 |
|         | 40                      | $0.0092 \pm 0.0023$                 | 0.9992 |
| IMD     | 10                      | $0.0632 \pm 0.0013$                 | 0.9976 |
|         | 20                      | $0.0408 \pm 0.0010$                 | 0.9967 |
|         | 30                      | $0.0323 \pm 0.0011$                 | 0.9936 |
|         | 40                      | $0.0237 \pm 0.0007$                 | 0.9997 |

which in turn led to the reduction of radical generation. Furthermore, high concentration of analyte blocked the reaching of photons to the photocatalyst which also affects the radical generation. Accordingly, the % degradation gets reduced at high initial concentrations. Thus, the lower initial concentration of TCS and IMD could enhance the % degradation.

### Catalyst dosage

In order to evaluate the effect of photocatalyst dose on the % degradation of TCS and IMD under UV light, the amounts of photocatalyst have been varied from 0.2 to 0.8 g/L and observed the upsurge in degradation efficiency of the catalyst for both the analytes at high concentrations, which are shown in Fig. 14. Under UV light exposure, the efficiency

of the ZnO-TS photocatalyst for TCS and IMD degradation was increased from 73.94 and 70.82 to 99.60% and 96.09%, respectively. The rate constants appraised from pseudo-first-order kinetic studies for degradation of TCS and IMD using ZnO-TS catalyst are compiled in Table 6. The high photocatalytic concentration provides the availability of high number of active sites for adsorption on the catalyst surface and thus boosted the radical generation, thereby increasing the photocatalytic efficiency of the catalyst.

### HPLC chromatogram analysis

The photocatalytic degradation of TCS and IMD was also confirmed through HPLC studies (Fig. 15). The HPLC chromatograms showed the retention times of TCS and IMD 7.827 min and 1.988 min, respectively. The photocatalytic degraded samples of IMD under optimized conditions were subjected to chromatographic analysis under conditions specified in experimental section, and the corresponding chromatograms are shown in Fig. 15(a–d). The slight shift of peak from 1.988 to 2.005 min retention time and decrease in intensity after 5-min irradiation of sample substantiate the initiation of degradation. Further, irradiation of sample resulted in the diminishing of peak corresponding to 1.988 min retention time along with the formation of by-products as assessed from the presence of new peaks at short retention time. The appearance of various additional peaks corresponding to short retention time has been gathered in table along with their corresponding intensity. However, peak analysis suggests almost

**Fig. 14** a, b Effect of ZnO-TS dose on photocatalytic degradation of TCS and IMD, and c, d pseudo-first-order kinetics plots

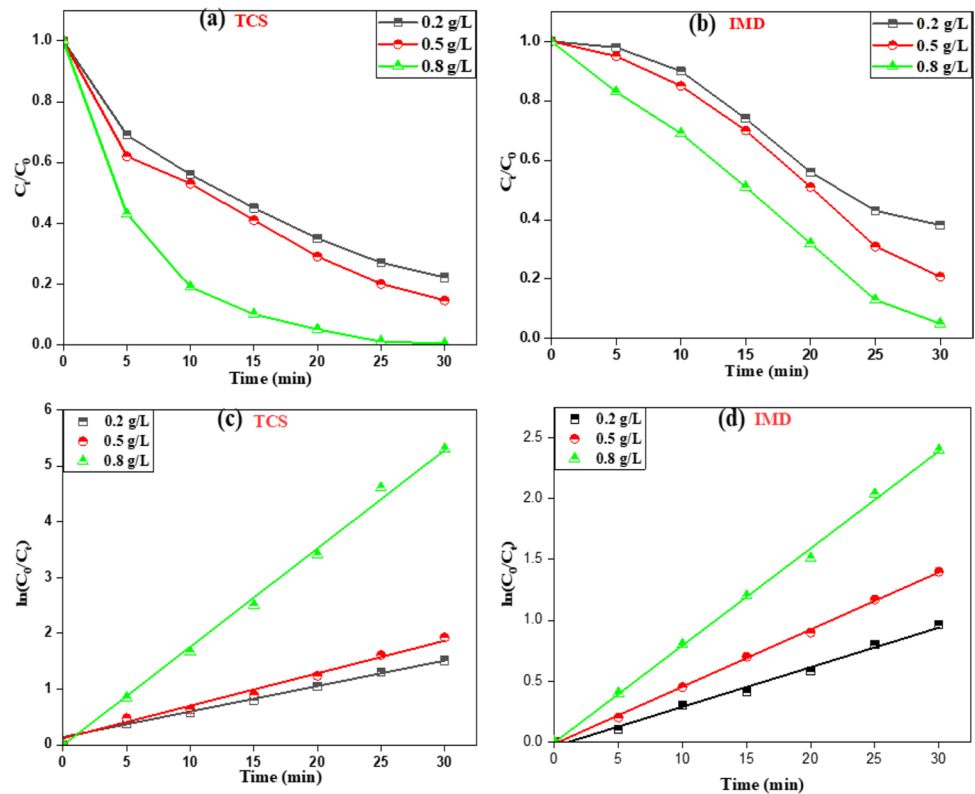


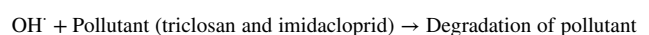
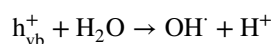
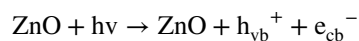
**Table 6** Represents the effect of catalyst dose on rate constant

| Analyte | Catalyst dose (g/L) | Rate constant ( $\text{min}^{-1}$ ) | $R^2$  |
|---------|---------------------|-------------------------------------|--------|
| TCS     | 0.2                 | $0.0462 \pm 0.0006$                 | 0.9991 |
|         | 0.5                 | $0.0621 \pm 0.0020$                 | 0.9894 |
|         | 0.8                 | $0.1759 \pm 0.0039$                 | 0.9982 |
| IMD     | 0.2                 | $0.0362 \pm 0.0013$                 | 0.9818 |
|         | 0.5                 | $0.0470 \pm 0.0006$                 | 0.9990 |
|         | 0.8                 | $0.0799 \pm 0.0014$                 | 0.9979 |

complete degradation of IMD as well as the intermediate formation after 5 min irradiation and, further, decreases in intensity of peaks of IMD and by-products have been observed after 25-min and 45-min (Fig. 15(b–d)) irradiation of UV light. Similarly, the chromatograms for photocatalytic degradation of triclosan are represented in Fig. 15(e–g). The decrease in intensity of parent peak, i.e., at 7.287 min retention time, has been noticed along with the formation of some additional peaks after 15 min of study; however, the intensity of by-products formed during the process gets decreased and results are summarized in Table 7.

## Mechanism

The mechanisms for photodegradation of triclosan and imidacloprid using different photocatalysts have been reported and shown in Fig. 16. The semiconductor's photoexcitation state involves the photoirradiation of ZnO, which led to the generation of electron–hole pair. Further, the photogenerated holes reacted with the surface hydroxyl groups and water molecules for the production of strong oxidizing species, i.e., hydroxyl radicals which catalyzed the reaction with the pollutant molecules that have to be degraded and resulted in the mineralization of pollutant moieties partially or completely (Schroder et al. 2020). However, the efficiency of the process is hampered by the reversible reaction, i.e., electron–hole combination which is expressed as follows (Chandra Pragada and Thalla 2021):



Additionally,  $\text{O}_2$  plays a vital role in photocatalytic process. The superoxide radicals produced due to the reduction

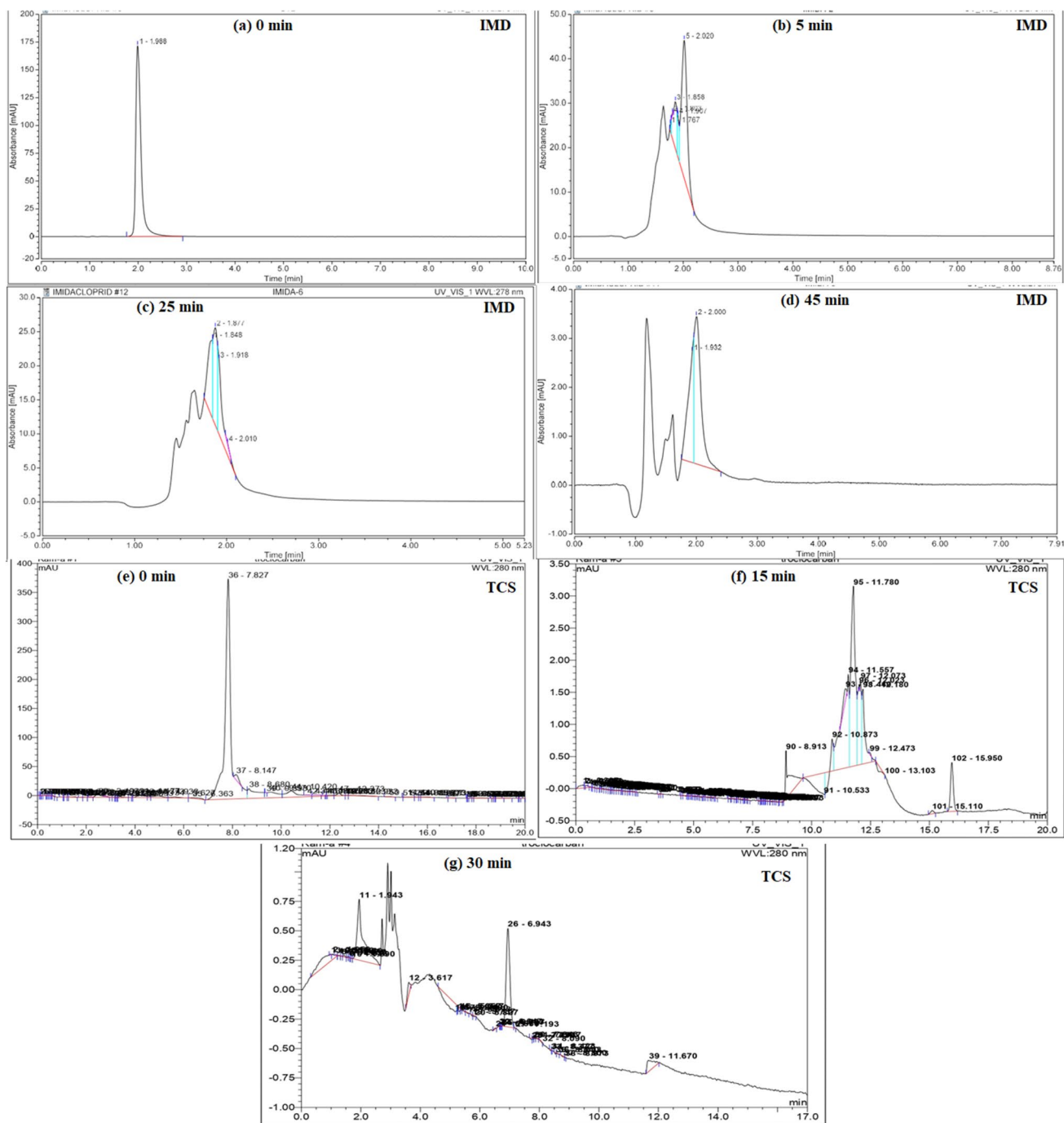


**Fig. 15** HPLC chromatograms of **a–d** IMD and **e–g** TCS degradation using ZnO-TS photocatalyst at different time intervals

of  $O_2$  by conduction band electrons led to the formation of hydroperoxyl radical along with other oxygen species like  $H_2O_2$  and OH which are highly reactive (Yang et al. 2020).

Conclusively, the formation of hydroxyl radicals, which are strong oxidants, is greatly accountable for the significant degradation efficiency of the nanosized ZnO for the degradation of emerging pollutants. Moreover, high surface of synthesized ZnO also accounts for the high % degradation.

### Recyclability of the catalyst

The stability of chemical features of the compound is an important factor to work efficiently as a photocatalyst and the stability of the catalyst can be tested by performing the reusability cycles. Figure 17 evinces the photocatalytic runs for TCS and IMD degradation for the evaluation of reusability of the catalyst. The efficiency of ZnO-TS photocatalyst has been appraised by



**Table 7** Summarizes the intensities of IMD and TCS corresponding to retention time at different time intervals

| Sample | Irradiation time (min) | Retention time (min) | Height (mAU) |
|--------|------------------------|----------------------|--------------|
| IMD    | 0                      | 1.988                | 172.524      |
|        | 5                      | 2.020                | 30.998       |
|        |                        | 1.907                | 9.423        |
|        |                        | 1.858                | 10.556       |
|        | 25                     | 1.918                | 14.338       |
|        |                        | 1.877                | 11.051       |
| 1.848  |                        | 11.700               |              |
| 45     | 2.000                  | 3.015                |              |
|        | 1.932                  | 2.264                |              |
|        | TCS                    | 0                    | 7.827        |
|        | 15                     | 7.8                  | 0.007        |
|        | 30                     | 7.8                  | 0.00         |

recovering the catalyst after each catalytic run. The insolubility of the catalyst in the analytic solution led to the easy separation by a centrifugation technique and the separated catalyst was washed several times with water–ethanol mixture and further utilized for the next catalytic runs. The results demonstrate that the photocatalyst exhibited the good regeneration and recyclability with no drastic change in % degradation of TCS and IMD up to nine consecutive runs. The gradual decrease in degradation efficiency of the ZnO-TS catalyst upon reuses attributed to the capturing of active sites due to interactions between photocatalyst and pollutant, i.e., TCS and IMD.

### Conclusion

Biopolymer XG-templated and template-free ZnO nanostructures have been synthesized using three different greener strategies, viz., sonochemical, hydrothermal, and mechanochemical

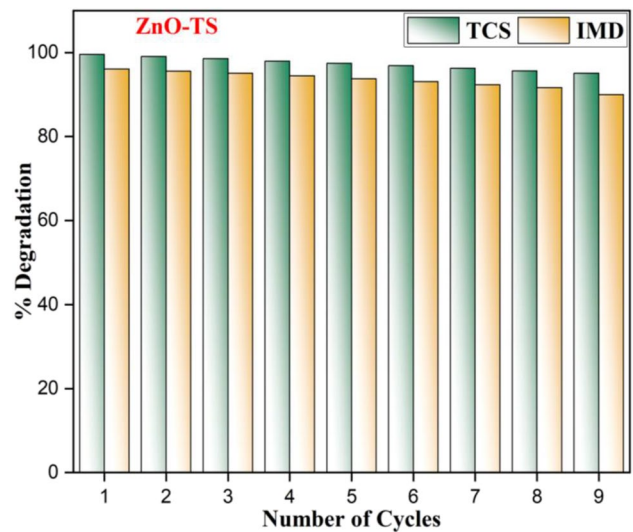
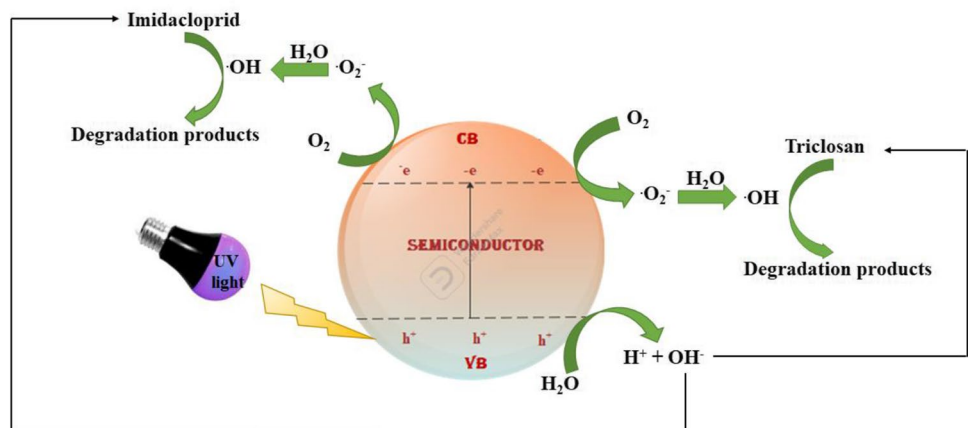


**Fig. 17** Reusability test for synthesized ZnO-TS nanostructures

methods. The template-assisted ZnO nanostructures served as a photoactive catalyst for the photocatalytic degradation of two emerging pollutants, i.e., TCS and IMD. The maximum degradation efficiencies 99.60% and 96.09% have been achieved for TCS and IMD, respectively, with pseudo-first-order rate constants  $0.173 \pm 0.005 \text{ min}^{-1}$  and  $0.101 \pm 0.007 \text{ min}^{-1}$ , employing ZnO-TS as a photocatalyst followed by ZnO-TH and ZnO-TM upon irradiation of UV light. HPLC data revealed the significant degradation capability of ZnO-TS catalyst for TCS and IMD which attributed to the low band gap energy, high surface area, and crystallinity, which in turn are responsible for the generation of highly reactive hydroxide radical species. Further, the detailed mechanistic aspects related to formation and subsequent degradation of by-products via various analytical techniques will be the future course of investigation; however, better photocatalytic performance of synthesised ZnO for phasing out the priority pollutant is well established.

**Fig. 16** Mechanism for photo-catalytic degradation of TCS and IMD



**Author contribution** All authors contributed to the study conception and design. Material preparation, data collection, and analysis were performed by Vidhi, Gagandeep Kaur, and Arshpreet Kaur. The first draft of the manuscript was written by Arshpreet Kaur and authors commented on previous versions of the manuscript. Dhiraj Sud read and approved the final manuscript.

**Data availability** All data generated or analysed during this study are included in this article.

## Declarations

**Ethical statement** This material is authors' own original work which has not been published elsewhere.

**Consent to participate** All authors declare that they participated in the study and development of the manuscript.

**Consent for publication** All authors read the final version of the manuscript and give consent for the article to be published.

**Competing interests** The authors declare no competing interests.

## References

- Alomair NA, Mohamed HH (2018) Green synthesis of ZnO hollow microspheres and ZnO/rGO nanocomposite using red rice husk extract and their photocatalytic performance. *Mater Res Express* 5:095012. <https://doi.org/10.1088/2053-1591/aaa469>
- Amulya MAS, Nagaswarupa HP, Kumar MRA, Ravikumar CR, Prashantha SC, Kusuma KB (2020) Sonochemical synthesis of NiFe<sub>2</sub>O<sub>4</sub> nanoparticles: characterization and their photocatalytic and electrochemical applications. *Appl Surf Sci* 1:100023. <https://doi.org/10.1016/j.apsadv.2020.100023>
- Bano K, Kaushal S, Singh PP (2021) A review on photocatalytic degradation of hazardous pesticides using heterojunctions. *Polyhedron* 209:115465. <https://doi.org/10.1016/j.poly.2021.115465>
- Braun PV, Osenar P, Twardowski M, Tew GN, Stupp SI (2005) Macroscopic nanotemplating of semiconductor films with hydrogen-bonded lyotropic liquid crystals. *ADV Funct Mater* 15:1745–1750. <https://doi.org/10.1002/adfm.200500083>
- Chandra Pragada S, Thalla AK (2021) Polymer-based immobilized Fe<sub>2</sub>O<sub>3</sub>-TiO<sub>2</sub>/PVP catalyst preparation method and the degradation of triclosan in treated greywater effluent by solar photocatalysis. *J Environ Manage* 29:113305. <https://doi.org/10.1016/j.jenvman.2021.113305>
- Gusain R, Gupta K, Joshi P, Khatri OP (2019) Adsorptive removal and photocatalytic degradation of organic pollutants using metal oxides and their composites: a comprehensive review. *Adv Colloid Interface Sci*. 102009. <https://doi.org/10.1016/j.cis.2019.102009>
- Hayati P, Mehrabadi Z, Karimi M, Janczak J, Mohammadi K, Mahmoudi G, Rostamnia S (2021) Photocatalytic activity of new nanostructures of an Ag(i) metal-organic framework (Ag-MOF) for the efficient degradation of MCPA and 2,4-D herbicides under sunlight irradiation. *New J Chem* 45:3408–3417. <https://doi.org/10.1039/d0nj02460k>
- Himanshi T, Harshita C, Hema B, Seema G (2022) Recent-enhancements in visible-light photocatalytic degradation of organochlorines pesticides: review. *Mater Today: Proc* 49:3289–3305. <https://doi.org/10.1016/j.matpr.2020.12.1036>
- Kaur A, Singh D, Sud D (2020) A review on grafted, crosslinked and composites of biopolymer Xanthan gum for phasing out synthetic dyes and toxic metal ions from aqueous solutions. *J Polym Res* 27. <https://doi.org/10.1007/s10965-020-02271-6>
- Kaur A, Bajaj B, Kaushik A, Saini A, Sud D (2022a) A review on template assisted synthesis of multi-functional metal oxide nanostructures: status and prospects. *Mater Sci Eng B* 286:116005. <https://doi.org/10.1016/j.mseb.2022.116005>
- Kaur A, Bajaj B, Sud D (2022b) Biopolymer xanthan gum templated facile synthesis of reusable cerium oxide nanoparticles as catalyst for reduction of nitroaromatic compounds. *J Iran Chem Soc* 19:4473–4489. <https://doi.org/10.1007/s13738-022-02616-6>
- Kaur A, Sud D (2022) Thionyl chloride facilitated polymerization of xanthan gum grafted copolymers for wastewater remediation by exclusion of synthetic dyes. *Polym Environ*. <https://doi.org/10.1007/s10924-022-02572-5>
- Khan N, Khan SU, Ahmed S, Farooqi, IH, Yousefi, M, Mohammadi (2019) Recent trends in disposal and treatment technologies of emerging-pollutants- a critical review. *Trends Anal Chem* 115744. <https://doi.org/10.1016/j.trac.2019.115744>
- Khatoun UT, Rao GN, Mohan MK, Ramanaviciene A (2018) Comparative study of antifungal activity of silver and gold nanoparticles synthesized by facile chemical approach. *J Environ Chem Eng* 6:5837–5844
- Kimling MC, Caruso RA (2012) Sol-gel synthesis of hierarchically porous TiO<sub>2</sub> beads using calcium alginate beads as sacrificial templates. *J Mater Chem* 22:4073–4082. <https://doi.org/10.1039/c2jm15720a>
- Son LL, Cuong ND, Van Thi TT, Hieu LT, Trung DD, Van HieuKonjac N (2019) glucomannan-templated synthesis of three-dimensional NiO nanostructures assembled from porous NiO nanoplates for gas sensors. *RSC Adv* 9:9584–9593. <https://doi.org/10.1039/c9ra00285e>
- Li JPH, Kennedy EM, Adesina AA, Stockenhuber M (2019a) Mechanistic insights into the Knoevenagel condensation reaction over ZnO catalysts: direct observation of surface intermediates using in situ FTIR. *J Catal* 369:157–167. <https://doi.org/10.1016/j.jcat.2018.10.039>
- Li Y, Zhang D, Ash J, Jia X, Leone A, Templeton A (2019b) Mechanism and impact of excipient incompatibility: crosslinking of Xanthan gum in pediatric powder-for-suspension formulations. *J Pharm Sci* 108:3609–3615. <https://doi.org/10.1016/j.xphs.2019.07.005>
- Lin J, Luo Z, Liu J, Li P (2018) Photocatalytic degradation of methylene blue in aqueous solution by using ZnO-SnO<sub>2</sub> nanocomposites. *Mater Sci Semicond Process* 87:24–31. <https://doi.org/10.1016/j.mssp.2018.07.003>
- Luo M, Huang Y, Zhu M, Tang Y, Ren T, Ren J, Li F (2018) Properties of different natural organic matter influence the adsorption and aggregation behavior of TiO<sub>2</sub> nanoparticles. *J. Saudi Chem Soc* 22:146–154. <https://doi.org/10.1016/j.jscs.2016.01.007>
- Maciak E, Opilski Z (2007) Transition metal oxides covered Pd film for optical H<sub>2</sub> gas detection. *Thin Solid Films* 515:8351–8355. <https://doi.org/10.1016/j.tsf.2007.03.022>
- Mansor ES, El Shall FN, Radwan EK (2022) Simultaneous decolorization of anionic and cationic dyes by 3D metal-free easily separable visible light active photocatalyst. *Environ Sci Pollut Res*. <https://doi.org/10.1007/s11356-022-22838-8>
- Masood MT, Qudisia S, Hadadian M, Weinberger C, Nyman M, Ahläng C, Smått JH (2020) Investigation of well-defined pinholes in TiO<sub>2</sub> electron selective layers used in planar heterojunction perovskite solar cells. *Nanomaterials* 10:181. <https://doi.org/10.3390/nano10010181>
- Mostafa H, Alireza M, Ramin N, Amir H, Shahram R, Kazem N (2021) A comprehensive systematic review of photocatalytic degradation of pesticides using nano TiO<sub>2</sub>. *Environ Sci Pollut Res* 28:13055–13071. <https://doi.org/10.1007/s11356-021-12576-8>
- Natsathaporn P, Jenjob R, Pattanasattayavong P, Yamsawas D, Crespy D (2020) Photocatalytic degradation of pesticides by nanofibrous membranes fabricated by colloidal-electrospinning. *Nanotechnology* 31:215603. <https://doi.org/10.1088/1361-6528/ab713d>
- Nidhin M, Indumathy R, Sreeram KJ, Nair BU (2008) Synthesis of iron oxide nanoparticles of narrow size distribution on polysaccharide templates. *Bull Mater Sci* 31:93–96. <https://doi.org/10.1007/s12034-008-0016-2>

- Otis G, Ejgenberg M, Mastai Y (2021a) Solvent-free mechanochemical synthesis of ZnO nanoparticles by high-energy ball milling of  $\epsilon$ -Zn(OH)<sub>2</sub> crystals. *Nanomaterials* 11:238. <https://doi.org/10.3390/nano11010238>
- Otis G, Ejgenberg M, Mastai Y (2021b) Solvent-free mechanochemical synthesis of ZnO nanoparticles by high-energy ball milling of  $\epsilon$ -Zn(OH)<sub>2</sub> crystals. *Nanomaterials* 11(1):238. <https://doi.org/10.3390/nano11010238>
- Pachiyappan J, Gnanasundaram N, Rao GL (2020) Preparation and characterization of ZnO, MgO and ZnO–MgO hybrid nanomaterials using green chemistry approach. *Results Mater* 7:100104. <https://doi.org/10.1016/j.rinma.2020.100104>
- Pineda A, Ojeda M, Romero AA, Balu AM, Luque R (2018) Mechanochemical synthesis of supported cobalt oxide nanoparticles on mesoporous materials as versatile bifunctional catalysts. *Microporous Mesoporous Mater* 272:129–136. <https://doi.org/10.1016/j.micromeso.2018.06.029>
- Radwan EK, Ibrahim MB, Adel A, Farouk M (2020) The occurrence and risk assessment of phenolic endocrine-disrupting chemicals in Egypt's drinking and source water. *Environ Sci Pollut Res* 27:1776–1788. <https://doi.org/10.1007/s11356-019-06887-0>
- Radwan EK, Ghafar HHA, Ibrahim MBM, Moursy AS (2022) Recent trends in treatment technologies of emerging contaminants. *Environ Qual Manag*. <https://doi.org/10.1002/tqem.21877>
- Rafi MM, Ahmed KSZ, Nazeer KP, Siva Kumar D, Thamilselvan M (2014) Synthesis, characterization and magnetic properties of hematite ( $\alpha$ -Fe<sub>2</sub>O<sub>3</sub>) nanoparticles on polysaccharide templates and their antibacterial activity. *Appl Nanosci* 5:515–520. <https://doi.org/10.1007/s13204-014-0344-z>
- Rodrigues J, Hatami T, Rosa Jorge M, Basile TE (2019) Photocatalytic degradation using ZnO for the treatment of RB 19 and RB 21 dyes in industrial effluents and mathematical modeling of the process. *Chem Eng Res Des* 153:294–305. <https://doi.org/10.1016/j.cherd.2019.10.021>
- Rupa EJ, Anandapadmanaban G, Mathiyalagan R, Yang D-C (2018) Synthesis of zinc oxide nanoparticles from immature fruits of *Rubus coreanus* and its catalytic activity for degradation of industrial dye. *Optik* 172:1179–1181
- Sabaghnia N, Janmohammadi M, Dalili M, Karimi Z, Rostamnia S (2019) Euphorbia leaf extract-assisted sustainable synthesis of Au NPs supported on exfoliated GO for superior activity on water purification: reduction of 4-NP and MB. *Environ Sci Pollut Res* 26:11719–11729. <https://doi.org/10.1007/s11356-019-04437-2>
- Samadi M, Zirak M, Naseri A, Kheirabadi M, Ebrahimi M, Moshfeh AZ (2019) Design and tailoring of one-dimensional ZnO nanomaterials for photocatalytic degradation of organic dyes: a review. *Res Chem Intermed* 45:2197–2254. <https://doi.org/10.1007/s11164-018-03729-5>
- Satdeve NS, Ugwekar RP, Bhanvase BA (2019) Ultrasound assisted preparation and characterization of Ag supported on ZnO nanoparticles for visible light degradation of methylene blue dye. *J Mol Liq* 291:111313. <https://doi.org/10.1016/j.molliq.2019.111313>
- Schmidt W, Eckhardt M, Wissner K, Lenk F, Grothe S, Kaskel J, Reineke S (2019) Efficiency of light outcoupling structures in organic light-emitting diodes: 2D TiO<sub>2</sub> array as a model system. *Adv Funct Mater* 29:1901748. <https://doi.org/10.1002/adfm.201901748>
- Schröder S, San-Román M-F, Ortiz I (2020) Photocatalytic transformation of triclosan. reaction products and kinetics. *Catalysts* 10:1468. <https://doi.org/10.3390/catal10121468>
- Singh YR, Kufitka I, Vilcakova J, Jamatia T, Machovsky M, Skoda D, Havlica J (2019a) Impact of sonochemical synthesis condition on the structural and physical properties of MnFe<sub>2</sub>O<sub>4</sub> spinel ferrite nanoparticles. *Ultrason Sonochem* 61:104839. <https://doi.org/10.1016/j.ultsonch.2019.104839>
- Singh, BK, Lee S, Na K (2019b) An overview on metal-related catalysts: metal oxides, nanoporous metals and supported metal nanoparticles on metal organic frameworks and zeolites. *Rare Metals* 1–16. <https://doi.org/10.1007/s12598-019-01205>
- Singha MK, Patra A (2020) Highly efficient and reusable ZnO microflower photocatalyst on stainless steel mesh under UV–Vis and natural sunlight. *Opt Mater*. 110000. <https://doi.org/10.1016/j.optmat.2020.110000>
- Solá-Gutiérrez C, Schröder S, San-Román MF, Ortiz I (2020) Critical review on the mechanistic photolytic and photocatalytic degradation of triclosan. *J Environ Manage* 260:110101. <https://doi.org/10.1016/j.jenvman.2020.110101>
- Suthakaran S, Dhanapandian, S, Krishnakumar, N, Ponpandian N (2020) Hydrothermal synthesis of surfactant assisted Zn doped SnO<sub>2</sub> nanoparticles with enhanced photocatalytic performance and energy storage performance. *J Phys Chem Solids* 109407. <https://doi.org/10.1016/j.jpics.2020.109407>
- Taghavi R, Rostamnia S, Farajzadeh M, Karimi-Maleh H, Wang J, Kim D, Jang HW, Luque R, Varma RS, Shokouhimehr M (2022) Magnetite metal-organic frameworks: applications in environmental remediation of heavy metals, organic contaminants, and other pollutants. *Inorg Chem* 61:15747–15783. <https://doi.org/10.1021/acs.inorgchem.2c01939>
- Takahashi K, Limmer SJ, Wang Y, Cao G (2004) Synthesis and electrochemical properties of single-crystal V<sub>2</sub>O<sub>5</sub> nanorod arrays by template-based electrodeposition. *J Phys Chem B* 108:9795–9800. <https://doi.org/10.1021/jp0491820>
- Vaiano V, Iervolino G, Rizzo L (2018) Cu-doped ZnO as efficient photocatalyst for the oxidation of arsenite to arsenate under visible light. *Appl Catal B* 238:471–479. <https://doi.org/10.1016/j.apcatb.2018.07.026>
- Velempini T, Prabakaran E, Pillay K (2021) Recent developments in the use of metal oxides for photocatalytic degradation of pharmaceutical pollutants in water—a review. *Mater Today Chem* 19:100380. <https://doi.org/10.1016/j.mtchem.2020.100380>
- Wang N, Chen J, Wang J, Feng J, Yan W (2019) Removal of methylene blue by polyaniline/TiO<sub>2</sub> hydrate: adsorption kinetic, isotherm and mechanism studies. *Powder Tech* 347:93–102. <https://doi.org/10.1016/j.powtec.2019.02.049>
- Wang Y, Ma C, Sun X, Li H (2002) Preparation and characterization of SnO<sub>2</sub> nanoparticles with a surfactant-mediated method. *Nanotechnology* 13:565–569. <https://doi.org/10.1088/0957-4484/13/5/304>
- Wu G, Zhang L, Cheng B, Xie T, Yuan X (2004) Synthesis of Eu<sub>2</sub>O<sub>3</sub> nanotube arrays through a facile sol–gel template approach. *J Am Chem Soc* 126:5976–5977. <https://doi.org/10.1021/ja039012l>
- Yang B, Zheng J, Li W, Wang R, Li D, Guo X, ... Jia X, (2020) Engineering Z-scheme TiO<sub>2</sub>-OV-BiOCl via oxygen vacancy for photocatalytic degradation of imidacloprid. *Dalton Trans*. <https://doi.org/10.1039/d0dt02128h>
- Zhang X, Sun H, Tan S, Gao J, Fu Y, Liu Z (2019) Hydrothermal synthesis of Ag nanoparticles on the nanocellulose and their antibacterial study. *Inorg Chem Commun* 100:44–50. <https://doi.org/10.1016/j.inoche.2018.12.012>
- Zhou Y, Schattka JH, Antonietti M (2004) Room-temperature ionic liquids as template to monolithic mesoporous silica with wormlike pores via a sol–gel nanocasting technique. *Nano Lett* 4:477–481. <https://doi.org/10.1021/nl025861f>

**Publisher's note** Springer Nature remains neutral with regard to jurisdictional claims in published maps and institutional affiliations.

Springer Nature or its licensor (e.g. a society or other partner) holds exclusive rights to this article under a publishing agreement with the author(s) or other rightsholder(s); author self-archiving of the accepted manuscript version of this article is solely governed by the terms of such publishing agreement and applicable law.